

Status of the Advanced Camera for Surveys

M. Clampin and G. Hartig

Space Telescope Science Institute, 3700 San Martin Drive, Baltimore, MD 21218

H. C. Ford, M. Sirianni, G. Meurer, A. Martel and J. P. Blakeslee

Department of Physics and Astronomy, The Johns Hopkins University, 3400 North Charles Street, Baltimore, MD 21218

G. D. Illingworth

UCO/Lick Observatory, University of California, Santa Cruz, CA 95064

J. Krist, R. Gilliland and R. Bohlin

Space Telescope Science Institute, 3700 San Martin Drive, Baltimore, MD 21218

Abstract. The Advanced Camera for Surveys (ACS), installed in the *Hubble Space Telescope* in March 2002, will significantly extend *HST*'s deep, survey imaging capabilities. ACS has met, or exceeded all of its key performance specifications. In this paper we present an introductory review of the in-flight performance of the instrument.

1. Introduction

The Advanced Camera for Surveys (ACS) is a third generation instrument for the *Hubble Space Telescope* (*HST*). It was installed in *HST* during the fourth servicing mission (SM3B) in March 2002. ACS replaced a first generation axial bay instrument, the Faint Object Camera (FOC). ACS has three channels, shown schematically in Figure 1, the Wide Field Camera (WFC), the High Resolution Camera (HRC) and the Solar Blind Camera (SBC). WFC is a high-throughput, wide field imager ($202'' \times 202''$) designed for deep imaging surveys in the near-IR. WFC provides a factor of 10 gain in discovery efficiency at 800 nm, compared to the Wide Field Planetary Camera-2 (WFPC2). In this context, discovery efficiency is defined as the product of field of view (FOV) and instrumental throughput. WFC is an f/25 camera which employs three reflective optics. The first mirror in the optical chain is a spherical mirror IM1, which images the *HST* pupil onto the mirror IM2. The mirror IM2 is an anamorphic asphere figured for the inverse conic error on the *HST* primary mirror, in order to correct spherical aberration on the *HST* primary, and field dependent astigmatism at the center of the ACS field of view. IM2 images onto mirror IM3, a Schmidt-like plate, which corrects astigmatism over the field of view, and images the beam through two filter wheels onto the WFC focal plane. The focal plane detector array is a mosaic of two Scientific Imaging Technologies (SITe) 2048×4096 CCDs (Sirianni et al. 2000, Clampin et al. 1998). The primary WFC design goal is to maximize the instrument throughput in the near-IR, and has been achieved by minimizing the number of optical elements in the design, and coating the mirrors with Denton protected-silver. The combined reflectivity of three silver coated mirrors at 800 nm is 98%, compared to 61% for three MgF₂ over coated aluminum mirrors. In the near-UV (>370 nm) the reflectivity of the silver coating falls rapidly. The

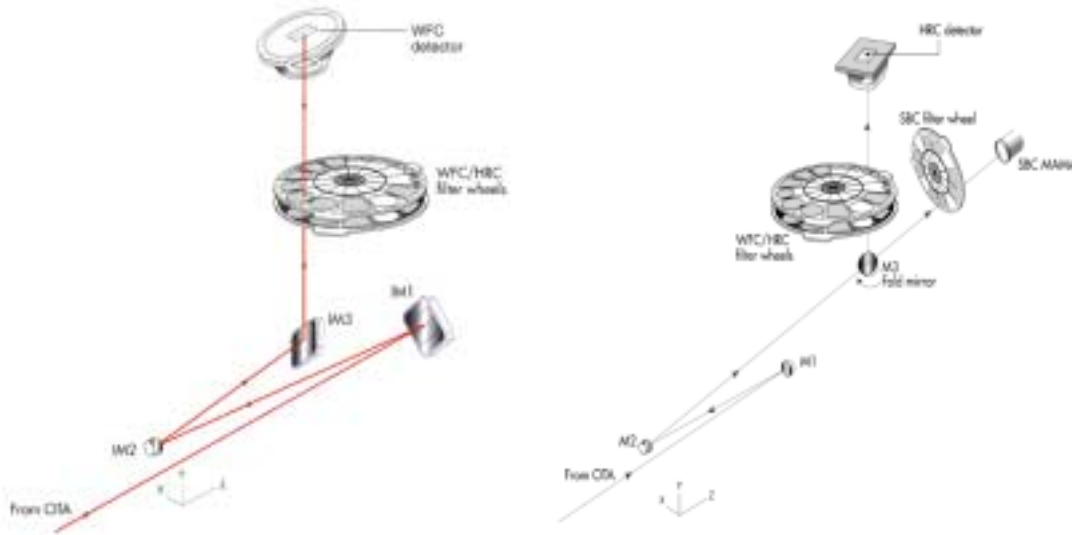


Figure 1. Schematic showing the optical designs for the WFC (left) and the HRC/SBC (right).

plate scale of the WFC is $0.05'' \text{ pixel}^{-1}$, which delivers near-critical sampling at the near-IR wavelengths for which the camera is optimized.

The HRC is a near-UV to near-IR imager, which provides critically sampled images in the visible, over a $29'' \times 26''$ field of view. HRC is also equipped with a true coronagraphic mode for high contrast imaging of the circumstellar environments of bright stars. HRC is a f/70 camera which shares two of its three mirrors with the SBC. The third mirror M3 is a fold mirror which is inserted into the beam to direct it through the two filter wheels onto the HRC focal plane array. The focal plane detector array is a SITE 1024×1024 CCD (Sirianni et al. 2000). The HRC shares the two filter wheels with the WFC and is capable of operating simultaneously with WFC. The HRC and SBC mirrors M1 and M2 are aluminum coated with MgF2 overcoating, and optimized for maximum reflectivity at 121.6 nm. The HRC mirror M3 is optimized for 200 nm and an incidence angle of 45° . The HRC focal plane detector is a SITE 1024×1024 CCD detector, based on the Space Telescope Imaging Spectrograph (STIS) CCD (Kimble et al. 1998). The HRC plate scale is $0.027'' \text{ pixel}^{-1}$, which yields fully sampled images in the visible. The SBC is selected when M3 is moved out of the light beam.

In order to maximize far-UV throughput, the SBC optical design is a two mirror optical system, with its own independent filter wheel. The SBC is a far-UV imager optimized for high throughput at 121.6 nm, with a field of view of $31'' \times 35''$, and a plate scale of $0.032'' \text{ pixel}^{-1}$. Its focal plane detector is a photon-counting CsI photocathode MAMA previously designated as the STIS flight spare detector.

2. Detectors

The ACS CCD detector systems are performing nominally. The detector read noise figures for WFC and HRC are summarized in Table 1. Both detector's are unchanged within their respective uncertainties, demonstrating the high degree of noise isolation achieved during ground testing, and the excellent on-orbit shielding from noise sources in the *HST*. Consequently, WFC broadband science observations will be typically, sky limited, while HRC science programs are read-noise limited, due to the smaller pixel size. The WFC

Table 1. Comparison of Pre-launch and Post-launch CCD Readout Noise

	Amp.	Gain	Read Noise e ⁻ RMS			Amp.	Gain	Read Noise e ⁻ RMS	
			pre	post				pre	post
WFC1	A	1	4.8	4.9	HRC	A	2	4.6	4.6
WFC1	B	1	4.7	4.8	HRC	B	2	4.4	4.7
WFC2	C	1	5.2	5.2	HRC	C	2	4.7	4.7
WFC2	D	1	4.7	4.8	HRC	D	2	5.0	4.9

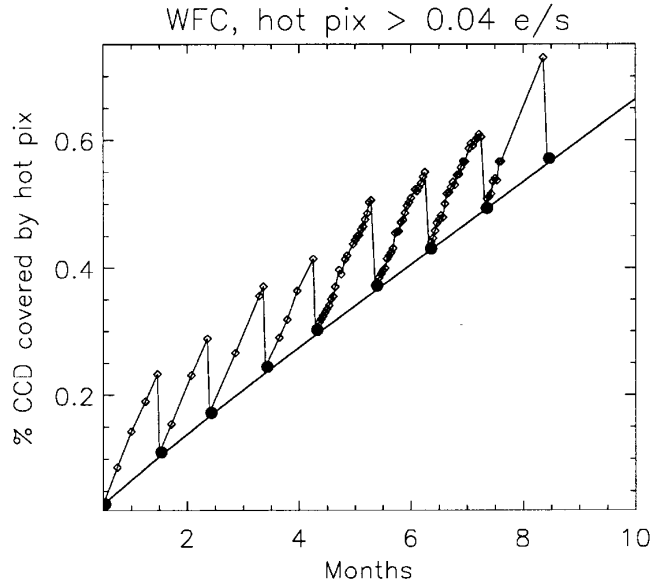


Figure 2. The growth of WFC hot pixels since launch from Riess (2002), illustrating the effect of monthly anneals on the long term evolution of hot pixels in the WFC. (Courtesy A. Riess 2002)

CCDs are read out simultaneously through all four amplifiers, while the HRC is read out through amplifier C.

The measured dark currents, excluding hot pixels ($>0.04 \text{ e}^- \text{ pixel}^{-1} \text{ s}^{-1}$) are $7.5 \text{ e}^- \text{ pixel}^{-1} \text{ s}^{-1}$ (-77°C) and $9.1 \text{ e}^- \text{ pixel}^{-1} \text{ s}^{-1}$ (-80°C), for the WFC and HRC respectively. These temperatures are achieved without the aft-shroud cooling system, which will be installed during the next (SM4) servicing mission. Hot pixels are a result of high energy proton displacement damage. The primary technique for moderating the hot pixel growth rate is annealing of the CCDs at the instrument's ambient "power off" temperature. Typically, the ACS detectors reach $\sim 20^\circ\text{C}$ when CCD cooling is switched off. The SBC's MAMA detector has also exceeded expectations for dark current, since pre-launch predictions of its operating temperature proved pessimistic. The SBC's measured dark current is 1.2×10^{-5} photons s^{-1} across the detector.

Hot pixel evolution has been evaluated over several ACS annealing cycles by Riess (2002). Hot pixels in the WFC appear at a rate of $\sim 1230 \text{ pixels day}^{-1}$. In Figure 2, we show the evolution of hot pixels and the effect of the monthly annealing. WFC hot pixels are annealed at a rate of $\sim 60\%$, in contrast to the factor of $\sim 80\%$ for the HRC detector. In subsequent WFC anneals, existing hot pixels are annealed at very low rates such that after 7 to 8 anneal cycles the cumulative fraction of annealed pixels reaches a plateau at $\sim 70\%$ (Riess 2002). Consequently, $\sim 1.5\%$ of the WFC mosaic will be covered by hot pixels after

24 months. This corresponds to the fraction of the WFC mosaic covered by cosmic rays in a 1000 second WFC exposure. The WFPC2 and STIS CCDs are similar to the HRC in annealing at a rate of $\sim 80\%$. Currently, the WFPC2 focal plane array has $\sim 2.5\%$ coverage by hot pixels, where WFPC2 hot pixels are defined as $>0.02 \text{ e}^- \text{ s}^{-1}$. While the WFC hot pixel evolution rate is a concern it can be handled during science operations by obtaining daily hot pixel calibration images, and dithering observations so that optimal combination of science frames can be used to eliminate hot pixels.

Initial post-launch measurements indicated that charge transfer efficiency (CTE) for the WFC and HRC detectors was consistent with pre-launch calibration data. CTE is expected to degrade with time since the radiation environment experienced in *HST*'s orbit has caused long-term degradation of CTE in previous *HST* instruments including STIS (Kimble et al. 2000), and WFPC2 (Whitmore et al. 1999). Preliminary calibration using the extended edge pixel response (EPER) method on internal WFC flat field images, indicates a degradation of parallel CTE from 0.999999 to 0.999991 (amplifier D) during the first six months of operation. EPER measurements help to track CTE degradation, but are not a good measure for assessing the scientific impact of CTE degradation observations. Observational factors such as the target size, density of sources in the field and sky background levels influence the impact of CTE on a given target.

3. Image Quality

The image quality for each of the three cameras is summarized in Table 2 from measurements by Hartig et al. (2002). In Figure 3 we show images of a star taken through the filters covering the spectral range of the WFC and HRC. The WFC F850LP image shows one artifact, a faint enhancement of the horizontal diffraction spike at wavelengths longer than $\sim 800 \text{ nm}$. In order to rectify the long wavelength halo observed in these CCDs (Sirianni et al. 1998), a reflective coating was applied to the frontside of the CCD prior to thinning. This coating appears to give rise to a diffraction artifact, which is seen in the F850LP image as an enhancement in the brightness in one of the four diffraction spikes.

Figure 5 shows the normalized, azimuthally averaged ACS and WFPC2 profiles for stars observed through a F555W filter. Although the ACS WFC and the WFPC2-PC cameras have very nearly the same physical and spatial pixel sizes, the WFPC2-PC half width at half maximum (HWHM) is $\sim 20\%$ narrower than the ACS WFC HWHM. This is likely due to slightly more charge diffusion in the backside-illuminated ACS pixels than in the frontside-illuminated WFPC2 pixels.

In the case of the HRC images in Figure 3, it can be seen that the NUV image through the F220W filter exhibits a small ‘‘spur.’’ The feature is independent of field position and is due to a moderate amount of several low order aberrations in the optical system. The aberration also impacts the SBC images so that at 122 nm they fall slightly below their specified encircled energy (EE), most likely as a combined result of this uncorrectable aberration, the large halo induced by the MAMA detector, and the mid-frequency figure error of the OTA optics. The SBC radius for $\text{EE} = 0.3$, derived from F125LP images of hot stars, is $0.06''$.

Figure 4 shows the encircled energy plots for the HRC and WFC point spread functions (PSFs) derived from F555W images. With allowance for telescope jitter, the WFC meets the image specification (Hartig et al. 2002). Even with image jitter included, the HRC exceeds the image specification. The encircled energy values for ACS and WFPC2 at 550 nm are also compared in Table 2. The WFPC2 values were taken from the *WFPC2 Instrument Handbook*. The ACS WFC and the WFPC2 PC have nearly the same angular pixel sizes ($0.050''$ and $0.046''$ respectively) and the same 50% and 80% EE values. Because the half width at half maximum (HWHM) is a better measure of image resolution than EE, Table 3 includes the HWHMs for the ACS and WFPC2 cameras derived from F555W

Table 2. Comparison of ACS and WFPC2 HWHMs and Encircled Energies at 555 nm

	ACS WFC (") pixels	WFPC2 WFC (") pixels	ACS HRC (") pixels	WFPC2 PC (") pixels
HWHM (Radius)	0.044	0.88	0.096	0.96
50% EE (Radius)	0.06	1.4	0.11	1.1
80% EE (Radius)	0.13	2.6	0.24	2.4

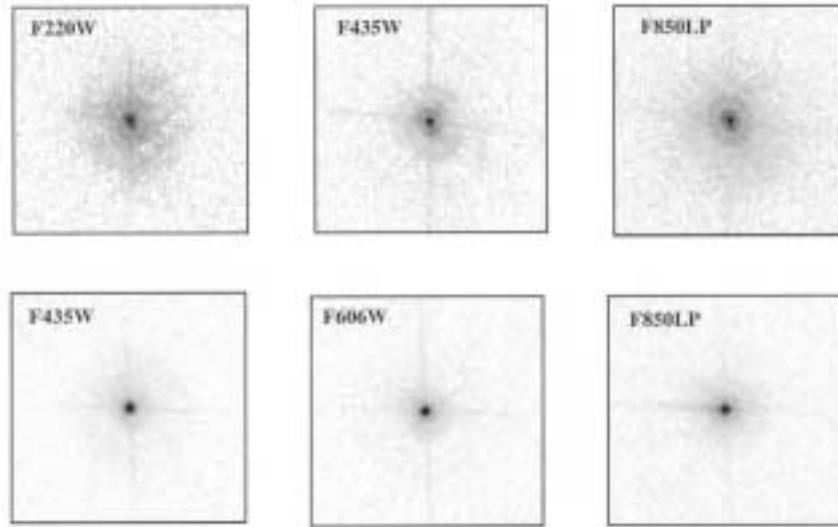


Figure 3. HRC images taken through the filters, F220W, F435W and F850LP are shown in the top three images ($3.3'' \times 3.3''$). The bottom three images show WFC images taken through F435W, F606W and F850LP ($5.9'' \times 5.9''$).

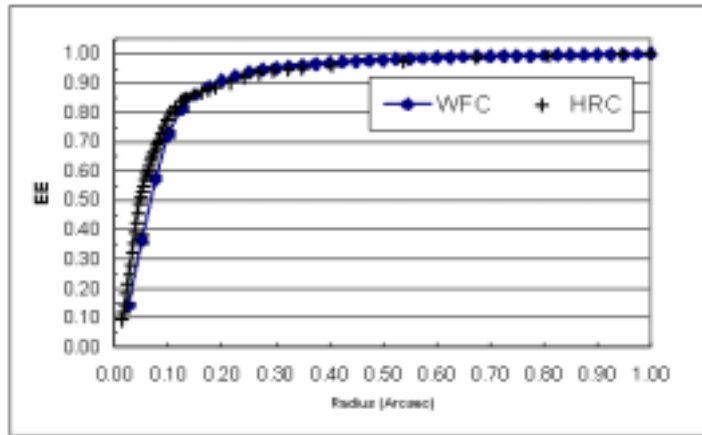


Figure 4. The fraction of the total light (“encircled energy” EE) enclosed within an aperture versus radius for WFC and HRC images of stars taken through an F555W filter.

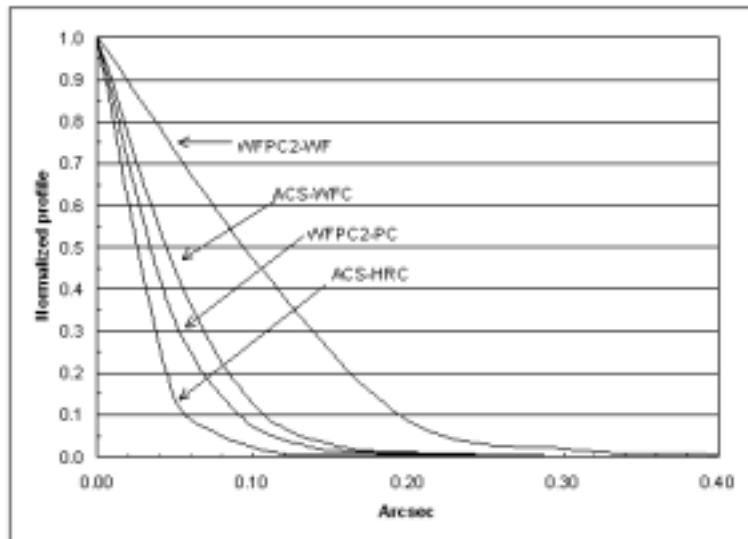


Figure 5. The normalized line profiles for ACS and WFPC2 PSFs derived from F555W images of stars. The profiles are “Moffat” profiles derived with the iraf task “imexamine.”

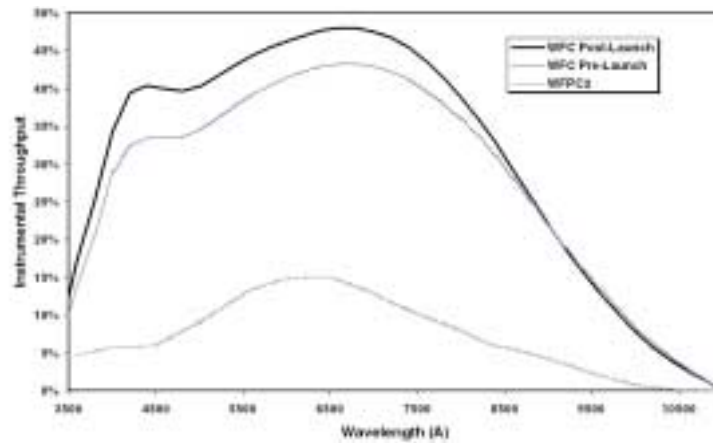


Figure 6. The net efficiency of the WFC plus the *HST* OTA versus wavelength. The predicted values were derived by combining the preflight component calibrations. The observed efficiency was derived from observations of standard stars used for on-orbit calibration of previous *HST* instruments.

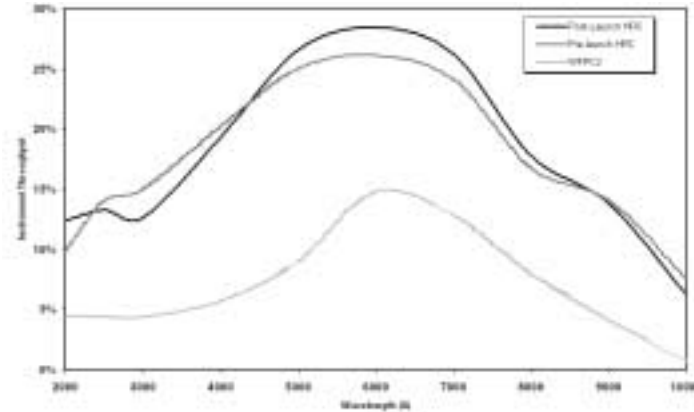


Figure 7. The net efficiency of the HRC plus the *HST* OTA versus wavelength. The observed sensitivity is 5 to 10% higher than predicted at wavelengths between 550 nm and 800 nm, and $\sim 25\%$ lower than predicted at 250 nm. In spite of the lower than expected sensitivity in the near ultraviolet, the HRC meets or exceeds its design specifications at all wavelengths.

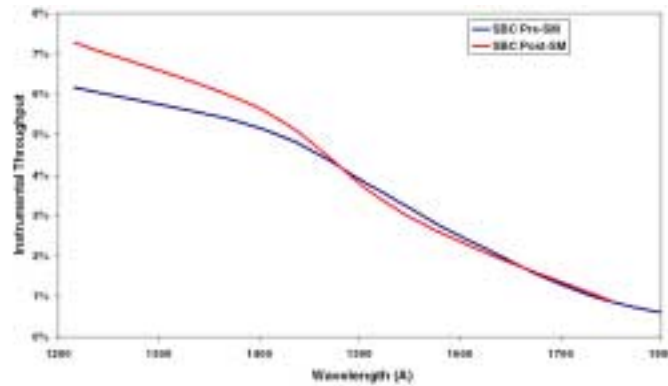


Figure 8. SBC plus *HST* OTA net efficiency versus wavelength. The predicted values were derived by combining the preflight component calibrations. The observed efficiency was derived from observations of standard stars used for on-orbit calibration of previous *HST* instruments.

images of stars. The Rayleigh criterion ($1.22\lambda/D$) for an unobstructed 2.4 aperture is $0.058''$ at 555 nm, and the full width at half maximum (FWHM) of the Airy function is $0.05''$. Table 2 shows that the observed ACS HRC FWHM is $0.05''$ (2 pixels). The HRC meets the design goal of being critically sampled at wavelengths $\lambda > 500$ nm.

4. Sensitivity

The on-orbit performance of the WFC exceeds the preflight predictions by a substantial margin. The pre-flight sensitivity of ACS was determined from component level measurements of the CCD quantum efficiencies, mirror reflectivities and filter throughputs. Systematic errors and measurement uncertainties are the most likely explanation for this unexpected gain in sensitivity. In Figure 6 we show the measured on-orbit net throughput of the WFC based on measurements of spectrophotometric standard stars through broad band filters. The WFC is near 50% overall efficiency at 650 nm. The HRC exhibited the same gain

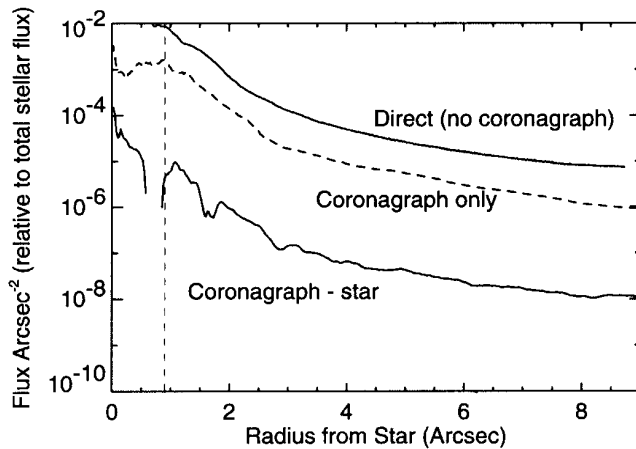


Figure 9. Radial surface brightness profiles of a star observed through the filter F435W. The top line is the predicted HRC profile (direct, no coronagraph). The middle line is with the coronagraph (1.8'' occulting spot), and the bottom line is the absolute value of the residual coronagraphic profile after the star is subtracted by an image of itself taken during a separate visit. Note that the Lyot stop in the coronagraph reduces the throughput by 53%.

in performance at visible wavelengths as the WFC, but showed a small decrease in NUV sensitivity compared to pre-launch predictions. The HRC measurements are shown in Figure 7. The SBC's peak net throughput is shown in Figure 8, with a comparison to STIS. The superior throughput of ACS results from the fact that it has only two reflections in the optical path to the SBC, compared to four in STIS.

5. ACS Coronagraph

The ACS HRC coronagraph comprises two opaque circular stops that are positioned in the *HST* aberrated focal plane and a Lyot stop that is simultaneously positioned immediately in front of the HRC M2 mirror, and thus close to the pupil image. The smallest stop has a diameter of 1.8'' and is positioned in the center of the HRC field. The largest stop has a diameter of 3.0'' and is 5.25'' from one edge of the HRC. The 1.8'' and 3.0'' spots block about 88% and 95% of the aberrated PSF, respectively. The Lyot stop reduces the throughput of non-occulted sources by $\sim 48\%$. In addition to the two circular stops, there is a 0.8'' wide opaque finger that extends 5.5'' over the HRC window at an angle of $\sim 74^\circ$ to the edge. Because the finger is not in the focal plane, there is a small amount of vignetting around its edges. During assembly of the ACS the tip of the finger was aligned with the center of the 3.0'' spot, with the goal of blocking light diffracted into the geometrical shadow from bright stars centered on the spot. However, after launch "gravity release" caused the finger and shadow of the large mask to misregister by $\sim 1''$.

Figure 9 shows the azimuthally averaged radial surface brightness profiles for a simulated direct F435W image of a star, the observed F435W profile when the star is centered on the small spot (1.8''), and the observed radial profile when two sequential coronagraphic images are subtracted. The simulated image includes diffraction from the *HST* pupil and from the residual polishing errors on the *HST* primary and secondary mirrors. The figure shows that the coronagraph reduces the background by ~ 6 . If a matching PSF is subtracted (e.g., by rolling the telescope and taking another image), the background is reduced by a factor of ~ 1000 .

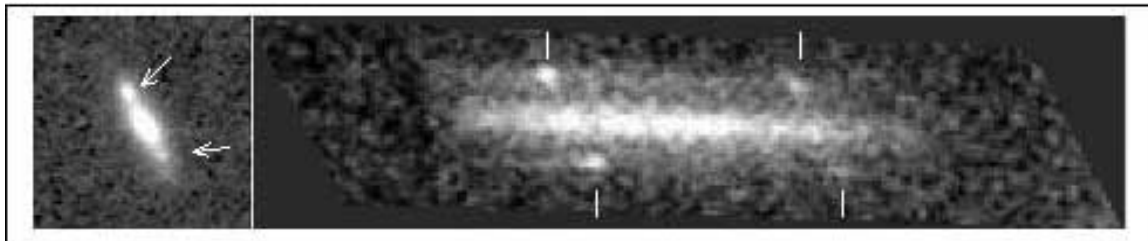


Figure 10. The left panel shows a 5-orbit direct image (2 orbits F775W + 3 orbits F850LP) image of an emission line galaxy in the HDFN. The F775W filter (Sloan i) includes the redshifted [OIII] $\lambda 5007$ emission line and the F850LP filter (Sloan z) includes redshifted $H\alpha$ emission. The right panel shows a 3-orbit grism image of the galaxy. The arrows mark the bright emission line regions in the image; the vertical lines mark the emission lines [OIII] $\lambda 5007$ and $H\alpha$ 6563 in the spectrum.

6. ACS Grism

The first order WFC dispersion, which depends on the position in the focal plane, varies from $3.63 \text{ nm pixel}^{-1}$ in one corner to $4.55 \text{ nm pixel}^{-1}$ in the other corner, with an average value of $3.95 \text{ nm pixel}^{-1}$. The spectral resolution is the product of the monochromatic FWHM and the dispersion. We assume that a monochromatic image has the same dimensions in the spatial and spectral directions. Table 3 gives the spatial and spectral resolution derived from an average of the five measurements at positions near the center and ends of the spectra. The resolution $R = \lambda/\delta\lambda$ varies from ~ 65 at the blue end of the spectrum to ~ 78 at the red end. The resolutions at 800 and 1000 nm are very close to the values for a diffraction-limited image sampled with $0.05''$ pixels. The spectral resolution achieved on extended sources will be proportional to the square root of the quadratic sum of the image size in the dispersion direction and the FWHM for a point source.

Table 3. ACS Grism Spectral and Spatial Resolution for Stellar Sources

Avg. Wavelength (nm)	Avg. Cross Dispersion FWHM (pixels)	Avg. Resolution (nm)	Resolution ($\lambda/\delta\lambda$)
593.8 ± 8.2	2.30 ± 0.2	9.07	65
801.6 ± 6.9	2.33 ± 0.3	9.21	87
977.6 ± 13.3	3.16 ± 0.7	12.49	78

Figure 10 shows a 5-orbit direct image (2 orbits F775W + 3 orbits F850LP) and a 3-orbit grism image of a galaxy in the HDFN13. The grism image shows that the prominent knots at each end of the galaxy are star forming regions with two strong emission lines ([OIII] $\lambda 5007$ and $H\alpha$ 6563). Figure 11 shows the spectra extracted at the positions of the two knots and the nucleus. The nucleus also shows strong emission at $H\alpha$. The observed wavelengths of the emission lines agree with the published redshift of the galaxy, $z = 0.319$. The grism's high sensitivity and low resolution make it particularly suitable for observations of stellar sources with broad spectral features, such as supernovae and brown dwarfs, and compact star forming regions that have strong emission lines.

Acknowledgments. ACS was developed under NASA contract NAS 5-32865, and this research is supported by NASA grant NAG5-7697. We are grateful for an equipment grant from the Sun Microsystems, Inc.

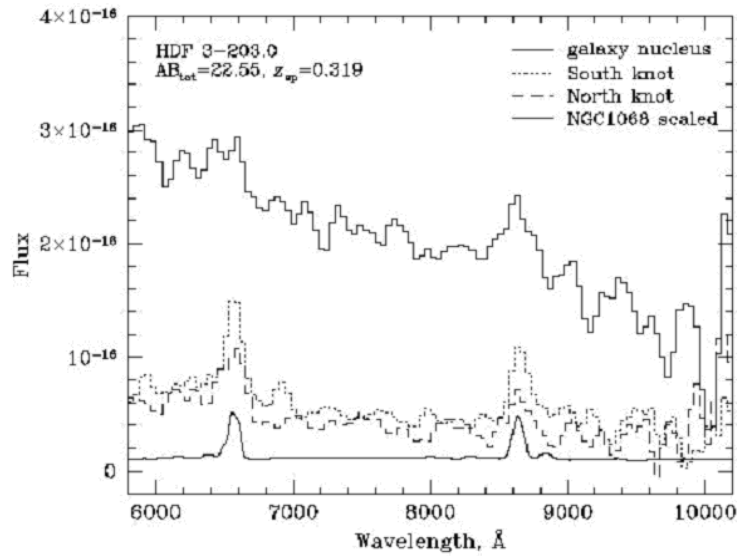


Figure 11. Spectra extracted from the grism image shown in Figure 10. The two strong emission lines in the knots at ~ 660 nm and 866 nm are [OIII] $\lambda 5007$ and H α 6563 at a redshift $z = 0.3229$.

References

- Clampin, M., et al. 1998, SPIE 3356, 332
 Hartig, G., et al. 2002, SPIE 4854, *in press*
 Kimble, R. A., Goudfrooij, P., & Gilliland, R. L. 2000, SPIE 4013, 532
 Kimble, R. A., et al. 1998, ApJ 492, L83
 Riess, A. 2002, *Instrument Science Report ACS 02-06* (Baltimore: STScI)
 Sirianni, M., et al. 2000, SPIE 4008, 669
 Sirianni, M., et al. 1998, SPIE 3355, 608
 Whitmore, B., Heyer, I., & Casertano, S. 1999, PASP 111, 1559